

Macromechanical behavior of oxide nanopowders during compaction processes

Boltachev G.Sh.^{1(*)}, Volkov N.B.¹, Kochurin E.A.¹, Maximenko A.L.², Shtern M.B.², Kirkova E.G.²

¹Institute of Electrophysics, Ural Branch of Russian Academy of Sciences, Amundsen Street 106, 620016, Ekaterinburg, Russia

²Frantsevich Institute for Problems of Materials Science, NAS Ukraine, Krzhizhanovsky Street 3, 03680, Kyev, Ukraine

*E-mail: grey@iep.uran.ru, tel.: +7(343)2678776

Abstract. Two granular systems (I and II) corresponding oxide nanopowders having different agglomeration tendency are simulated by the granular dynamics method. The particle size is 10 nanometer. The interaction of particles involves the elastic forces of repulsion, the tangential forces of "friction", the dispersion forces of attraction, and in the case of II system the opportunity of creation/destruction of hard bonds of chemical nature. The processes of the uniaxial compaction, the biaxial (radial) one, the isotropic one, the compaction combined with shear deformation as well as the simple shear deformation are studied. The effect of the positive dilatancy is found out in the processes of shear deformation. The loading surfaces of nanopowders are constructed in the space of stress tensor invariants, i.e., the hydrostatic pressure and the deviator intensity. It is revealed that the form of the loading surfaces is similar to an ellipse, which is shifted along the hydrostatic axis to compressive pressures. The associated flow rule is analyzed. The nonorthogonality of the deformation vectors to the loading surface is established in the both systems modeled.

Keywords: nanopowder, granular dynamics method, loading surface, associated flow rule.

I. Introduction

At present time high hopes concerning the development of promising structural and functional materials are pinned on the production and the investigation of nanostructured ceramics based on different oxides, for example, Al_2O_3 , ZrO_2 , Y_2O_3 , YSZ, and so on [1, 2, 3, 4, 5]. The powder metallurgy methods, which include such stages as the nanopowder production, compaction, and sintering, are the most debugged and fruitful methods for manufacture of the nanosized ceramic materials [2, 3, 4, 5, 6, 7]. The nanostructure preservation during the sintering stage needs the use of reduced temperatures that makes great demands of compacts prepared in previous stage [2, 3, 4, 5]. Generally, the compacts must be uniform and have large density. On the other hand, the size effect in the compaction processes is known. It is harder to compact the nanopowders as compared to the powders consisting of larger size particles in view of the presence of relatively large adhesion forces [8, 9, 10, 11], which result from dispersion forces of attraction [12, 13, 14, 15]. To overcome the strong adhesion of nanopowders it is necessary to use very high pressures, which can turned out beyond the ultimate strength of experimental setup [16]. Such high pressures are achieved, for example, in the processes of magnetic pulsed compaction owing to the application of inertial effects [7]. In spite of the considerable experimental progress in this line [2, 3, 4, 5], it can be claimed that the further progress is impeded by the lack of theoretical description of nanosized powders.

As a rule, present-day theoretical approaches to nanopowder description are the application of principles, which have developed for larger particle powders and do not take into account the peculiarities of new subjects of inquiry. So, for example, the theory of the plastically hardening porous body [6, 7, 17] and the related models of sintering and hot-pressing [18, 19] appear to be the powerful tools for the theoretical analysis. On the whole, the results of such models have been verified experimentally for the processes of the cold compaction of the powders consisting of micron- (or larger) size particles [6, 18, 19]. In the case of the cold compaction the plasticity theory of the materials having the volume compressibility has been applied. Here, as a rule, they suppose that the behavior of bodies being compacted can be describe in terms of the yield stress and the deformation hardening both on a macroscopic scale and on a particle scale. In the case of nanosized powders, especially of oxide ones, where the particles cannot deform plastically [8, 20], such conceptions as the yield stress or hardening takes very relative meaning. As a result, the adaptability of the continuous theory requires additional vindications at the least. On the other hand, the sophisticated analysis and revision of continuous theories are impossible without a lot of laborious experiments, which should provide additional information on subjects of inquiry (nanosized powders).

The granular dynamics method (or discrete element method) suggested for the first time by Cundall and Strack [21] and being developed strongly at present time [12, 13, 14, 15, 22, 23, 24, 25, 26, 27, 28, 29, 30] is a convenient alternative to real and laborious experiments and is a very promising approach, which allows

finding the detailed information on powder systems. Due to a great extent of the sphericity and the non-deformability (strength) of individual particles of oxide nanopowders being studied, the granular dynamics method is particularly attractive and promising tool of the theoretical analysis. The low plastic deformability of particles with size of 10 – 100 nm is connected with their defects free: the dislocations are ejected from the particles by the high "image" forces [20]. This kind of particles (especially oxide nanoparticles) is elastically deformed with unloading shape recovery. Within the bounds of the granular dynamics this fact allows us to avoid the difficulties related to accounting the plastic deformation of individual particles. Thus we emphasize that the simulation presented in this study can be used to describe the behavior of granular systems where the appearance of the plastic shape change of particles can be neglected (like oxide nanopowders).

This paper is a continuation of the investigations [13, 14, 15]. References [13, 14] were devoted to 2D simulations. In Ref. [15] the discrete three-dimensional model of oxide nanopowders was developed. Using this model we succeeded in reproducing the known properties of different alumina-based nanopowders. In this study two monodisperse systems corresponding oxide nanopowders having weak (system I) and strong (system II) agglomeration tendency are simulated. The numerical experiments are formulated in 3D geometry: the particles of the model systems have a spherical shape with diameter $d = 10$ nm and possess both translation and rotation degrees of freedom. In addition to the contact interaction laws commonly used, the interaction of particles involves the dispersion forces of attraction and in the case of II system the opportunity of creation/destruction of hard interparticle bonds. These bonds appear as a result of hard pressing force between particles which is initiated or by action of high dispersion interaction or by compaction process, Ref. [15].

II. Calculation procedure

The model cell is a right-angle prism with sizes of x_{cell} , y_{cell} and z_{cell} . For initial packing generation the algorithm defined in Ref. [15] is used, which allows us to create isotropic and uniform structures in a form of the connected 3D-periodic cluster with chains thickness of 2 particles. The total number of particles N_p is 8000, the initial density ρ_0 is 0.24. The density ρ is a relative volume of the solid phase, that is $\rho = (\pi/6)N_p d^3 / V_{cell}$, where V_{cell} is the model cell volume. The periodic boundary conditions are used on all the faces of the cell. The system deformation is carried out by simultaneous changes of selected sizes of the model cell and proportional rescaling of the appropriate coordinates of all the particles. After every act of deforming the new equilibrium location of the particles is determined. This procedure corresponds to the quasi-static conditions of the powder compaction.

The stress tensor σ_{ij} averaged over the model cell was calculated by the known expression [22, 23, 24]

$$\sigma_{ij} = \frac{-1}{V_{cell}} \sum_{k < l} f_i^{(kl)} r_j^{(kl)}, \quad (1)$$

where the summation is performed over all the pairs of the interacting particles k and l ; $\vec{f}^{(kl)}$ is the total force effecting the particle k from the particle l ; $\vec{r}^{(kl)}$ is the vector connecting the centers of the considered particles. The interaction forces between particles are described by the relationships [15]:

$$f_a(r) = \frac{\pi^2}{3} \frac{(nd_0^3)^2 \varepsilon d^6}{(r + \alpha d_0)^3 [(r + \alpha d_0)^2 - d^2]^2}, \quad r = |\vec{r}|, \quad (2)$$

$$\frac{f_e(r)}{Ed^2} = \frac{(h/d)^{3/2}}{3(1-\nu^2)} - \frac{\pi}{4} \frac{k_r(1-\nu)}{(1-2\nu)(1+\nu)} \left[\frac{h}{d} + \ln \left(1 - \frac{h}{d} \right) \right], \quad h = d - r, \quad (3)$$

$$f_t(\delta) = \min \left\{ \frac{4Ea\delta}{(2-\nu)(1+\nu)}; \mu f_e; \pi a^2 \sigma_b \right\}, \quad a = \frac{\sqrt{hd}}{2}, \quad (4)$$

$$M_p(\theta_p) = \min \left\{ \frac{8Ea^3}{3(1+\nu)} \theta_p; \mu M(a); \frac{\pi}{2} a^3 \sigma_b \right\}, \quad M(a) = -2\pi \int_0^a \sigma_n(r) r^2 dr, \quad (5)$$

$$M_r(\theta_r) = \min \left\{ \frac{4}{3} \frac{Ea^3}{1-\nu^2} \theta_r; \frac{1}{3} a f_e \right\}. \quad (6)$$

Here: the modified Hamaker formula (2) determines the dispersive attraction force f_a ; the modified Hertz law (3) gives the elastic repulsive force f_e ; the linearized Cattaneo–Mindlin law (4) defines tangential interaction of the pressed particles (forces of "friction"); the linearized Jäger law (5) (or the Reissner-Sagoci law, Ref. [31]) describes the surface forces moment M_p arising under the rotation of the pressed particles about the contact

axis at the angle θ_p ; the Lurie law (6) is the surface forces moment M_r arising under the bending of the contact axis at the angle θ_r (only in the presence of hard interparticle bond; Ref. [32], page 272, Eq. (4.5)). In the Eqs. (2)–(6): ε and d_0 are the power and dimensional parameters of the intermolecular forces; α is the coefficient determining the minimum gap between the contacting particles (at $r = d$) and thus specifying the maximum force of attraction ($f_{a,\max} = f_a(d)$); E and ν are the Young modulus and the Poisson ratio of the particles; δ is the tangential displacement of the contact area; a is the contact area radius; μ is the friction coefficient; σ_b is the critical shear stress defining the material shear strength; σ_n is the normal stress on the contact surface.

Creation/destruction of the hard interparticle bond is described by the parameter Δr_{ch} characterizing the necessary interparticle pressing force [15]. It is assumed that the decrease of distance r between the particle centers up to the value $r_{\min} \leq d - \Delta r_{ch}$ initiates the hard bond creation. After the creation of the hard interparticle bond the further compression (as r decreases) continues to obey the elastic interaction law (3) and at the extension (as r increases) we have linear relationship between the force f_e and the distance r up to the distance $r' = r_{\min} + \Delta r_{ch}$. For distances $r > r'$ the partial contact destruction is introduced and described by the increase of the parameter r_{\min} so that the difference $r - r_{\min}$ should remain equal to its maximum value Δr_{ch} . The total destruction of the interparticle contact occurred at the extension up to the distance $r = d$. The restrictions in Eqs. (4) and (5) related to the friction coefficient μ are removed with creation of the hard interparticle bond.

Alumina in the α -phase is implied as the particle material for which we accept: $E = 382$ GPa, $\nu = 0.25$, $nd_0^3 = \sqrt{2}$, $d_0 = 0.392$ nm; $\varepsilon = 1224k_B$, $\sigma_b = 0.018E$ [15]. Simulations are performed for two model monodisperse systems with particle diameter $d = 10$ nm. The model system I with the parameters $\alpha = 0.37$ and $\mu = 0.13$ is characterized by the absence of the hard interparticle bonds (an unreal high value equal d is assigned to the parameter Δr_{ch}) and corresponds to the weakly agglomerating powder of Ref. [15]. In the model system II with the parameters $\alpha = 0.24$, $\mu = 0.10$ and $\Delta r_{ch} = 0.008d$ the opportunity of the hard interparticle bond creation is taken into account. This system corresponds to the strongly agglomerating powder of Ref. [14]. Larger value of the interparticle gap (α) and the suppression of agglomeration in I system are due to the adsorbate presence on the particle surface.

We carried out the computer experiments for the following processes:

A. The uniform (triaxial) compression: on the every deformation step of the model cell all its sizes decreased simultaneously by 0.1% from the current values. In this case, the strain rate tensor e_{ij} and stress tensor σ_{ij} are spherical tensors, that is $e_{ij} = (e/3)\delta_{ij}$, $\sigma_{ij} = \sigma_z\delta_{ij}$ (δ_{ij} is the unit tensor, $e = \text{Tr}(e_{ij})$).

B. The biaxial compression along the axes Oy and Oz . The strain rate and stress tensors are characterized by the values $e_{xx} = 0$, $e_{yy} = e_{zz} = e/2$; $\sigma_{xx} \neq \sigma_{yy} = \sigma_{zz}$. For deviator intensity of the strain rate tensor $\gamma = \sqrt{\gamma_{ij}\gamma_{ji}}$ ($\gamma_{ij} = e_{ij} - (e/3)\delta_{ij}$) we have $\gamma = |e|\sqrt{1/6}$, and for deviator intensity of the stress tensor $\tau = \sqrt{\tau_{ij}\tau_{ji}}$ ($\tau_{ij} = \sigma_{ij} - \delta_{ij} \text{Tr}(\sigma_{ij})/3$) we have $\tau = |\sigma_{xx} - \sigma_{zz}|\sqrt{2/3}$.

C. The uniaxial compression along the axis Oz : $e_{xx} = e_{yy} = 0$, $e_{zz} = e$; $\sigma_{zz} < 0$, $\sigma_{xx} = \sigma_{yy} = \sigma_t$; $\gamma = |e|\sqrt{2/3}$, $\tau = |\sigma_t - \sigma_{zz}|\sqrt{2/3}$.

D. The z -compression combined with application of the shear deformation: the simultaneous compression in the Oz direction (the value z_{cell} decreased by 0.1% from the current value) and the extension in the Oy direction (the value y_{cell} increased by 0.05% from the current value) were carried out on the every deformation step. The strain rate tensor is characterized by the values: $e_{xx} = 0$, $e_{yy} = -e$, $e_{zz} = 2e$; $\gamma = |e|\sqrt{14/3}$.

E. The shear deformation of the model cell at constant volume. Here the value z_{cell} decreased and the value y_{cell} increased simultaneously (by 0.1% from the current values) on the every deformation step: $e_{xx} = 0$, $e_{yy} = -e_{zz}$; $e = 0$, $\gamma = |e_{yy}|\sqrt{2}$.

III. Extraction of "elasto-reversible" part

In the calculations with compression (the processes A–D) the model cell compaction was carried out up to the prescribed level p_{max} of the external load along the axis Oz . Then unloading of the model cell was performed, during which the cell was expanded in all directions with the rates proportional to the corresponding stresses: $e_{ii} \propto \sigma_{ii}$. This stage (the elastic unloading [27]) is characterized by the density change $\Delta\rho_{el}$. Apparently, besides purely elastic unloading of interparticle contacts the pressure unloading is also accompanied by irreversible processes of relative particle displacement. So naming these stages "elastic" is rather relative and implies only that the elastic processes here dominate. The elastic unloading calculations were performed for the values $p_{max} = 0.025, 0.05, 0.1, 0.2, 0.3, 0.5, 0.7, 1, 1.5, 2, 3, 4$ and 5 GPa. The relationship between the applied external pressure $p_{out} = -\sigma_{zz}$ and the value $\Delta\rho_{el}$ was approximated by the expressions

$$p_{out} = s_1\Delta\rho_{el} + s_2\Delta\rho_{el}^2 + \frac{s_3\Delta\rho_{el}}{(s_4 + \Delta\rho_{el})^2}. \quad (7)$$

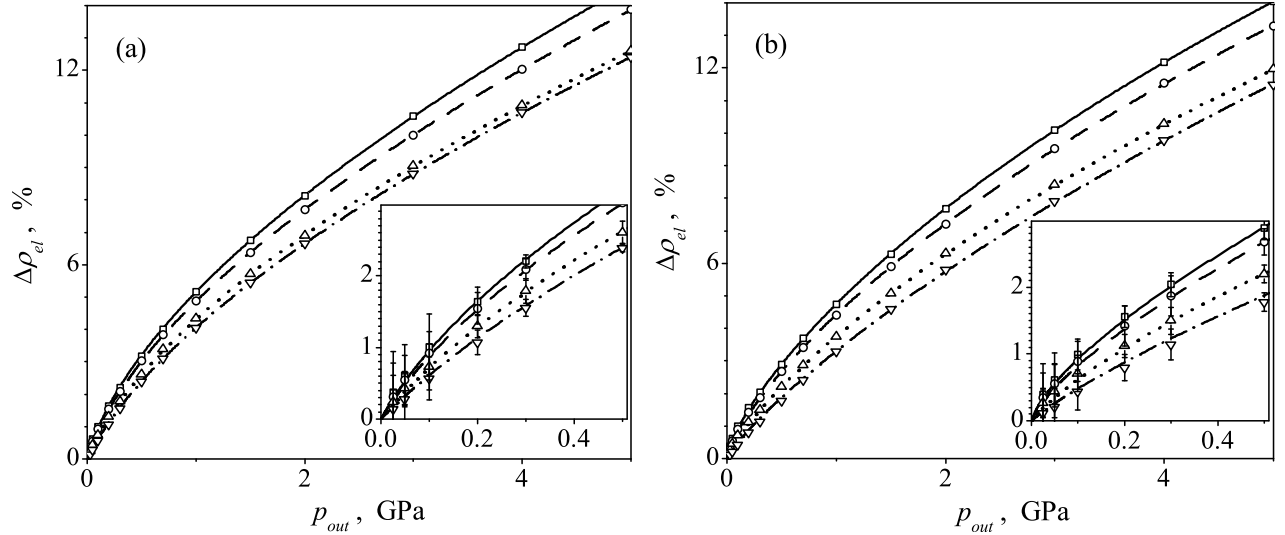


Figure 1: Density change during elastic unloading ($\Delta\rho_{el} = \rho_p - \rho_u$) versus external pressure $p_{out} = -\sigma_{zz}$ for systems I (a) and II (b). Points correspond to the simulation results and lines correspond to the approximations by Eq. (7) for the processes A (solid lines, squares), B (dashed lines, circles), C (dotted lines, upper triangles), and D (dash-and-dot lines, lower triangles). The insets show the low pressure zones in an enlarged scale.

Approximation coefficients for system I: $s_1 = 24.3$, $s_2 = 104.1$ (the process A); $s_1 = 25.3$, $s_2 = 118.4$ (the process B); $s_1 = 28.1$, $s_2 = 140.7$ (the process C); $s_1 = 30.8$, $s_2 = 126.2$ (the process D); and $s_3 = -0.65$, $s_4 = 0.2$ for all the processes. Approximation coefficients for system II: $s_1 = 16.0$, $s_2 = 142.0$ (the process A); $s_1 = 17.7$, $s_2 = 151.9$ (the process B); $s_1 = 22.7$, $s_2 = 163.6$ (the process C); $s_1 = 28.3$, $s_2 = 135.3$ (the process D); and $s_3 = -0.01$, $s_4 = 0.03$ for all the processes. Figure 1 shows that the suggested approximations describe the calculated data with the error, which is not more than the statistical averaging error (each of the calculations consisted of 10 independent computer experiments). The inverse relations $\Delta\rho_{el}(p_{out})$ presented in the figure demonstrate nonlinear behavior, which appears with the greatest distinction for system II in the low pressure zones. On the whole, presence of the hard bonds in system II leads to rather smaller values $\Delta\rho_{el}$ that relates to suppression of the irreversible processes of particle sliding (rearrangement) during the elastic unloading stage. It should be noticed, however, that the differences are not large. Thus, for the uniform compression processes (A) at the pressure $p_{out} = 1$ GPa we have $\Delta\rho_{el} = 5.2\%$ in the system I and 4.7% in the system II.

Obtained relations (7) allow us to extract elasto-reversible part ($\Delta\rho_{el}$) from the total strain of the model cell and to isolate irreversible (plastic) component which is characterized by the material unloading density ρ_u . The unloading density dependences on the external pressure for the analyzed systems are represented in Fig. 2. For comparison the initial dependences $\rho_p(p_{out})$ with the elastic contribution ($\rho_p = \rho_u + \Delta\rho_{el}$) are also represented there. Interestingly enough that in the both systems the dependences $\rho(p)$ corresponding to the different processes (A–D) are rather close to each other and the maximum difference of the unloading densities is within 1-2%. On the whole, absence of the hard interparticle bonds in system I leads to its higher compactability: the curves $\rho_p(p_{out})$ and $\rho_u(p_{out})$ pass above for the system I. But in the high pressure zone the curve $\rho_p(p_{out})$ differences become insignificant and large values of the elastic unloading ($\Delta\rho_{el}$) for the system I lead to a slight decrease of the unloading density as compared with system II. For example, in the case of the uniform compression at the pressure $p_{out} = 5$ GPa we have $\rho_p = 76.4\%$, $\rho_u = 61.7\%$ in system I and $\rho_p = 76.3\%$, $\rho_u = 62.3\%$ in system II. In the hypothetical limit of the unrestrictedly large pressures ($p \rightarrow \infty$) the powder unloading density is about 65% (see insertions in Fig. 2). The average coordination number k of the simulated systems after unloading from $p_{max} = 5$ GPa is in the range 6.2–6.4 for the processes A–D. Thus, it can be concluded that after the unloading from high values of the external pressure ($p_{out} > 5$ GPa) the systems being studied are close to the random close packing (RCP) state, for which $\rho \simeq 0.64$ and $k \simeq 6$.

Qualitatively the dependences $\rho_u(p_{out})$ for systems I and II demonstrate similarities. On the curves $\rho_u(p_{out})$ we can identify three qualitative stages which are known from experiments [33, 34] and two-dimensional computer simulations [24] of micron-size powder compaction. In the first stage the density weakly depends on the pressure. Here the external loading is insufficient to overcome initial particle bonds. This stage corresponds to the pressure $p_{out} < 9$ MPa in system I and $p_{out} < 20$ MPa in system II. An active densification by the law $\Delta\rho \propto \ln(p_{out})$ is

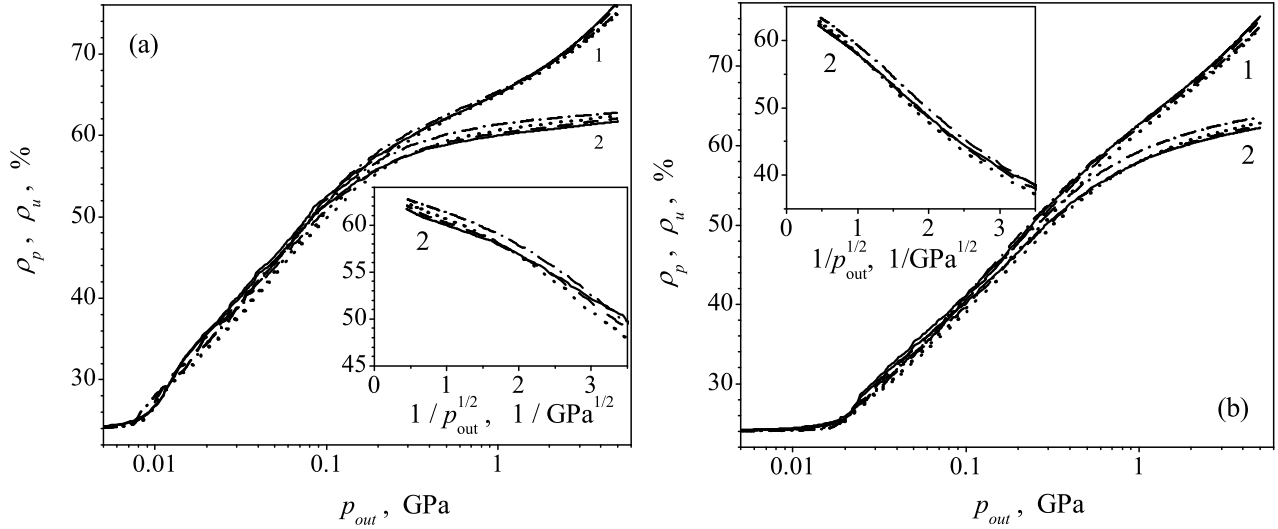


Figure 2: Density ρ_p (under pressure) /1/ and unloading density ρ_u /2/ versus external pressure p_{out} for the processes A–D (lines are marked by the same symbols as in Fig. 1) in systems I (a) and II (b). The insets show the unloading density versus value of $p_{out}^{-1/2}$.

Table 1: Calculation parameters for simulations of the model cell shear deformation as well as the densities for systems I and II at the shear stages.

No.	n_z	L_n/d	L_0/d	N_p	I : $\rho, \%$	II : $\rho, \%$
1	4	14	12	6000	36.1	35.6
2	3	14	12	5000	37.6	37.2
3	3	14	12	6000	45.0	44.3
4	3	14	12	7000	52.1	51.0
5	3	14	12	8000	58.1	56.9
6	3	14	12	9000	60.5	60.4
7	2	15	13	5000	39.5	38.9
8	2	15	13	6000	47.1	46.4
9	2	15	13	7000	54.3	53.5
10	2	15	13	8000	59.5	58.4
11	2	18	15	8000	41.1	40.3

observed in the second stage. Here the basic processes of particle rearrangement take place. In the third stage when $p_{out} \gtrsim 200$ MPa in system I and $p_{out} \gtrsim 500$ MPa in system II the powder unloading density gradually reaches some maximum value $\rho_{u,max}$ about 65%. The calculations show that here we have $p_{out} \propto 1/(\rho_{u,max} - \rho_u)^2$ (see insertions in Fig. 2). It should be noted that in two-dimensional structure simulations the respective power exponent is equal to one [24, 35], which allows us to suppose in the general case $p_{out} \propto 1/(\rho_{u,max} - \rho_u)^{D-1}$, where D is the space dimension.

IV. Shear deformation at constant volume

In simulations of the shear deformation the initial sizes of the model cell were determined equal to $x_{cell} = y_{cell} = L_n$, $z_{cell} = (n_z + 1)L_n$ ($n_z \geq 2$). At first, the uniform compression of the model cell was carried out up to the specified sizes ($L_n \rightarrow L_0$). This step allowed us to obtain the powder structure with the necessary initial density ρ_0 . Then the unloading (not large reverse cell expansion) was performed. After that, the shear deformation process was carried out: the model cell was compressed along the axis Oz and elongated along the axis Oy so that the volume remained constant. The process was stopped when the values $z_{cell} = L_0$ and $y_{cell} = (n_z + 1)L_0$ were reached. At last, the re-unloading till zero stresses was carried out.

These calculations have been performed for 11 parameter sets (n_z, L_n, L_0, N_p) which are listed in Table 1. In the first unloading stage (after the initial uniform compression of the cell) the significant density decrease is

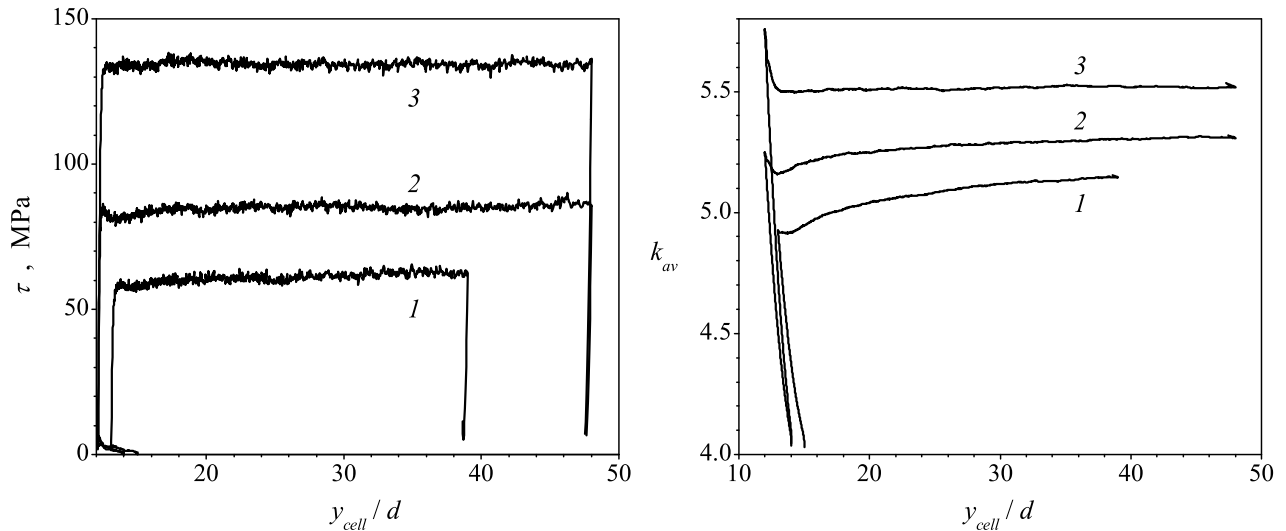


Figure 3: Stress deviator intensity versus model cell size y_{cell} in the simulation of shear deformation for the system II with parameter sets (see Table 1) No. 7 /line 1/, 3 /2/ and 4 /3/.

Figure 4: Average coordination number versus model cell size y_{cell} in the simulation of shear deformation for the system II. Lines are marked by the same symbols as in Fig. 3.

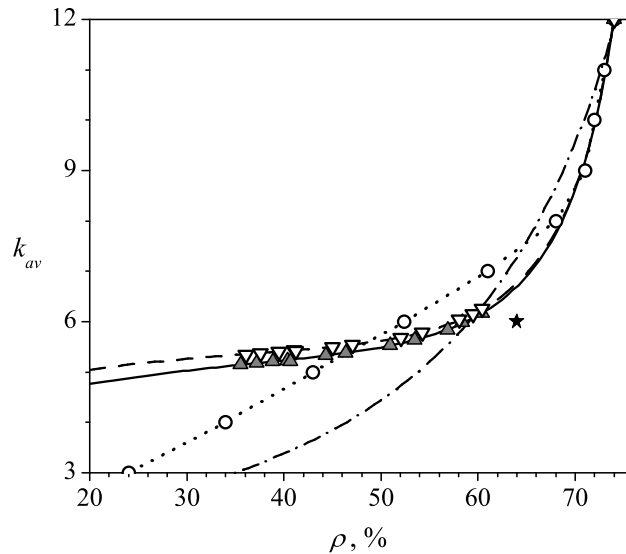


Figure 5: Average coordination number k_{av} versus density under simple shear deformation. Triangles are the simulation data for model systems I (light) and II (dark); circles are the data for the regular packing [36]; asterisk is the RCP state [25]; dot-and-dash line is relation (9) presented in Ref. [33].

observed, and it is different for analyzed systems I and II. Obtained densities of these systems, characterizing the shear deformation stages at constant volume (at constant density), are also represented in Table 1. Density changes in the final unloading stages are negligibly small.

Figures 3 and 4 demonstrate the behavior of selected properties of the model cell (the stress deviator intensity and the average coordination number for system II) versus the cell size y_{cell} . As can be seen, for the parameter set No. 7 (lines 1) the duration of the simulation process, i.e. value n_z , is insufficient for the foolproof reaching of the critical (stationary) state. It should be noted that this set corresponds to the density $\rho = 39\%$. Density increase contributes to faster reaching of the stationary state. For instance, in the case of set No. 4 (lines 3 in the figures) $\rho = 51\%$ and the state of the model cell reaches constant values almost immediately.

To determinate the values characterizing the critical state, the dependences on y_{cell} of all analyzing param-

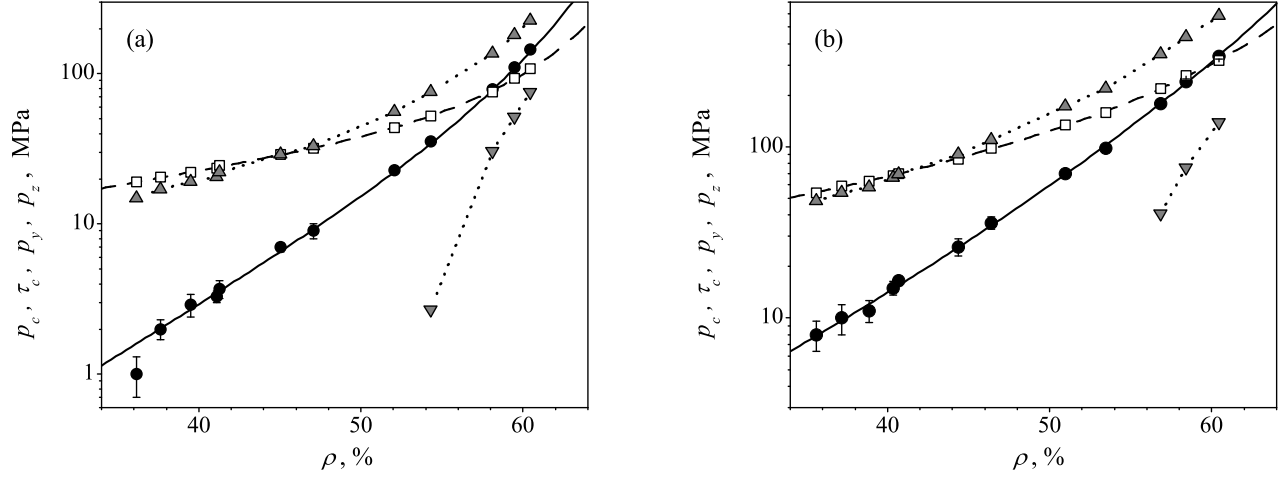


Figure 6: Stress deviator intensity τ_c (light squares, dashed lines), hydrostatic pressure p_c (dark circles, solid lines), minimum pressure $p_y = -\sigma_{yy}$ (down triangles), and maximum pressure $p_z = -\sigma_{zz}$ (up triangles) versus powder body density under simple shear deformation for the system I (a) and II (b). Points are the simulation data, lines for τ_c and p_c are the approximations by Eq. (10).

eters at range of $y_{cell} > 20d$ were approximated by the expression $f(y_{cell}) = f_c + f_1 y_{cell}^{-2} + f_2 y_{cell}^{-3}$. Figure 5 presents the obtained values of the average coordination number k_{av} versus powder body density in the critical state. Calculated points for both model systems is approximated by the dependence

$$k_{av} = k_{av,1} + k_{av,2}\rho + k_{av,3}\rho^2 + \frac{k_{av,4}}{\rho_* - \rho}, \quad (8)$$

with coefficients: $k_{av,1} = 3.326$, $k_{av,2} = 4.145$ (system I); $k_{av,1} = 2.943$, $k_{av,2} = 4.648$ (system II); $k_{av,3} = -8.888$, $k_{av,4} = 0.765$, $\rho_* = 0.813$. In addition to the calculated points, the condition $k_{av}(0.74) = 12$ was assumed for the approximations (8). Besides our calculated data, the data of regular 3D-structure density [36], the RCP parameters [25], and the relation

$$k_{av} = \frac{\pi/2}{(1 - \rho)^{3/2}} \quad (9)$$

proposed in Ref. [33] are given in the same figure for comparison. The figure shows that in examined density range (30-60%) the calculated values of coordination numbers rather weakly depend on density in contrast to regular structure coordination numbers or the relation (9). The dependences $k_{av}(\rho)$ of two model systems are close to each other but difference between them (about 0.2) exceeds the calculated error by an order. At that, system I (without hard bonds) is characterized by larger values of the coordination numbers.

Figure 6 presents the critical (stationary) values of the stress deviator intensity τ_c , the hydrostatic pressure p_c , and the minimum and maximum components of the stress tensor ($p_y = -\sigma_{yy}$ and $p_z = -\sigma_{zz}$) versus the density of the examined systems. Since logarithmic scale is used along the ordinate axis, the minimum stress components (p_y) are shown only for large densities where they have positive values. The same as for the average coordination number, the calculation points in Fig. 6 are fitted satisfactorily by the common curves. This indicates that the realized algorithm allows us to obtain the critical state reliable enough. The critical state is only determined by the model system density and does not depend on such calculation parameters as the particle number N_p , the model cell size L_0 , and the duration of the simulation process n_z . The simulation results for the invariants τ_c and p_c in Fig. 6 are approximated by expressions

$$\ln(\tau_c/p_*) = \tau_1 + \tau_2\rho + \tau_3\rho^2 + \frac{\tau_4}{\rho_{lim} - \rho}, \quad \ln(p_c/p_*) = p_1 + p_2\rho + p_3\rho^2 + \frac{p_4}{\rho_{lim} - \rho}, \quad (10)$$

where $\tau_1 = -0.533$, $\tau_2 = 7.966$, $\tau_3 = -10.951$, $\tau_4 = 0.916$, $p_1 = -6.637$, $p_2 = 17.525$, $p_3 = -8.296$, $p_4 = 0.837$ (for the system I); $\tau_1 = 2.649$, $\tau_2 = 0.666$, $\tau_3 = 3.379$, $\tau_4 = 0.310$, $p_1 = -2.102$, $p_2 = 8.963$, $p_3 = 4.393$, $p_4 = 0.190$ (for the system II); and $p_* = 1$ MPa, $\rho_{lim} = 0.813$. Fig. 6 shows that the examined structures (oxide nanopowders) have noticeable positive dilatancy: they tend to increase their volume under simple shear stress. In our case, it results in positive values of the hydrostatic pressure. As the density grows the dilatancy increases

too. Whereas the pressure p_c is significantly lower than the tangential stress level τ_c at densities $\rho < 50\%$, we have already $p_c > \tau_c$ at high densities ($\rho > 60\%$).

Comparison the ratio p_c/τ_c in systems I and II shows that the creation of hard interparticle bonds notably increases dilatancy in the low density region. For instance, at $\rho \simeq 36\%$ this ratio in system I is 0.05 while in system II it is almost three times larger (0.14). However, as the density increases, the values of p_c/τ_c in systems I and II are rapidly move to each other and become equal (about 0.7) at $\rho = 55\%$. At larger densities the system I (without hard bonds) already demonstrates larger values of the ratio p_c/τ_c in comparison to the system II. While absolute values of the hydrostatic pressure in the system I remains smaller than in the system II.

Maximum components of the stress tensor (p_z) represented in Fig. 6 are significantly lower than the axial pressures ($p_{out} = p_z$) in the processes A–D analyzed in the previous section. Evidently, in both systems (I and II) the increase of the shear deformation contribution makes the powder compaction easier. For example, at the density $\rho_u = 60\%$ the simulation results for the examined processes are $p_z = 210$ /process E/, 480 /D/, 690 /C/, 830 /B/, 1010 /A/ (in MPa, system I); $p_z = 550$ /E/, 1200 /D/, 1600 /C/, 1750 /B/, 1830 /A/ (in MPa, system II). The pressures p_z , which are necessary for shear deformation initiation in the E-process, could be considered as a lower limit of the external forces required for reaching the assigned density.

V. Loading surface

The loading surface is a key parameter of the powder body for describing its mechanical properties within continuum approach. It determines the boundary of initiation the plastic-irreversible deformation processes. In contrast to plastically incompressible materials, in particular, compact metals, the powder loading surface is determined not only by the stress deviator intensity (τ) but also the first invariant of the stress tensor (p). Moreover, its position in the $p - \tau$ plane depends on the current density (or the porosity $\theta = 1 - \rho$) and tends to the yield condition of solid material at $\theta \rightarrow 0$. To describe the behavior of porous bodies, which reaction to the change of the load sign can be neglected, many researchers use the approximation of the loading surface in the form of [6, 17, 19]:

$$\frac{p^2}{\Psi(\theta)} + \frac{\tau^2}{\phi(\theta)} = (1 - \theta)\tau_0^2(\Gamma_0), \quad (11)$$

where τ_0 is the yield stress of solid phase, Γ_0 is the effective shear strain in it,

$$\Gamma_0 = \int \gamma_0 dt, \quad \gamma_0^2(1 - \theta) = \Psi(\theta) e^2 + \phi(\theta) \gamma^2, \quad (12)$$

e and γ are the trace and the deviator intensity of the macroscopic strain rate tensor, respectively, and the porous functions Ψ and ϕ are defined within the hydrodynamic analogy of the elasticity theory [18, 37]. The hardening rule $\tau_0(\Gamma_0)$ should be determined empirically, for instance, by the experimental curves of uniaxial compression. While stresses reach the surface (11), the deformation behavior is defined by the associated rule. It requires the orthogonality of the strain rate vector to the loading surface in the stress space [6]. This leads to the requirement of deviator coaxiality for the tensors e_{ij} and σ_{ij} and, with regard to the surface (11), to the scalar relation

$$\Psi e \tau = -\phi \gamma p. \quad (13)$$

For a given deformation conditions the relations (11) and (13) allow us to express any of the stress tensor components as a function of density (porosity). In the case of analyzed processes for axial pressure $p_{out} = -\sigma_{zz}$ we have

$$\mathbf{A}: \quad p_{out} = \sqrt{\Psi} \sqrt{1 - \theta} \tau_0(\Gamma_0), \quad \Gamma_0 = \int_{\theta}^{\theta_0} \sqrt{\Psi} \frac{d\theta}{(1 - \theta)^{3/2}}, \quad (14)$$

$$\mathbf{B}: \quad p_{out} = \sqrt{\Psi + \frac{1}{6}\phi} \sqrt{1 - \theta} \tau_0(\Gamma_0), \quad \Gamma_0 = \int_{\theta}^{\theta_0} \sqrt{\Psi + \frac{1}{6}\phi} \frac{d\theta}{(1 - \theta)^{3/2}}, \quad (15)$$

$$\mathbf{C}: \quad p_{out} = \sqrt{\Psi + \frac{2}{3}\phi} \sqrt{1 - \theta} \tau_0(\Gamma_0), \quad \Gamma_0 = \int_{\theta}^{\theta_0} \sqrt{\Psi + \frac{2}{3}\phi} \frac{d\theta}{(1 - \theta)^{3/2}}, \quad (16)$$

$$\mathbf{D}: \quad p_{out} = \left(\Psi + \frac{5}{3}\phi \right) \sqrt{\frac{3(1 - \theta)}{3\Psi + 14\phi}} \tau_0(\Gamma_0), \quad \Gamma_0 = \int_{\theta}^{\theta_0} \sqrt{\Psi + \frac{14}{3}\phi} \frac{d\theta}{(1 - \theta)^{3/2}}. \quad (17)$$

This expressions show that the relation $p_{out}(\theta)$ should significantly depend on the pressure conditions. Estimations, represented in Ref. [15], show that the definition of the hardening rule $\tau_0(\Gamma_0)$ on the base of the uniaxial

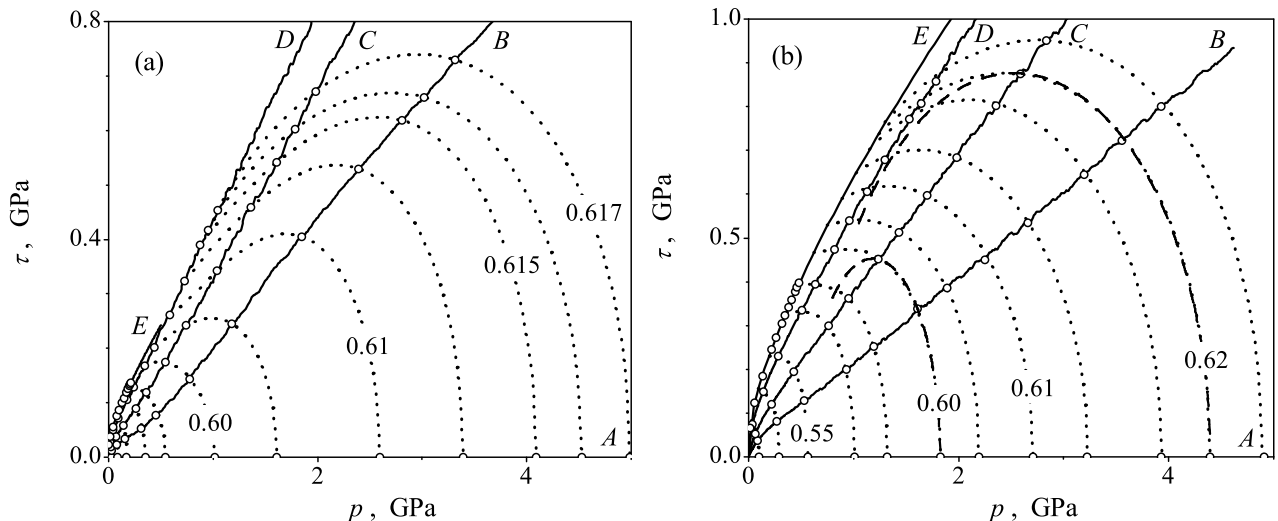


Figure 7: Stress deviator intensity versus hydrostatic pressure for the system I (a) and II (b). Solid lines: monotonic loading curves for the processes A–D (line A coincides with the abscissa axis) and line $\tau_c(p_c)$ of the E process. Dotted lines: loading surface (19) at constant density values $\rho_u = 40, 50, 55, 58, 59, 60, 60.5, 61\%$ (in both systems), and also 61.3, 61.5, 61.6, 61.7% for the system I and 61.4, 61.8, 62, 62.2% for the system II. Dashed lines for the system II are loading surfaces (18) at values $\rho_u = 60$ and 62%.

compression curve (process C) gives density differences about 10% according to the equations (14) and (16) for the system I at the pressure $p_{out} = 100$ MPa. The calculated curves in Fig. 2 demonstrate at this pressure one order less difference on the density. It is about 1%.

Inapplicability of the loading surface (11) to the systems examined is also conformed by the dilatancy effect detected in the previous section. Symmetry of the surface (11) relative to the deviator axis presupposes absence of the dilatancy. In particular, Eq. (13) shows that the value p should become zero under the condition $e = 0$ (shear deformation without compaction, E process).

These evidences identify the difference between powder and porous bodies: the powder relatively weakly resists the tensile strains. As a result, the loading surface locates in the right part of the $p - \tau$ plane. In contrast to the powder, the sintered porous body is characterized by presence of the created interparticle contacts, which leads to its equal resistance to the tensile and compression strains. Thus, identified incompatibility of the mechanical properties of the modeled powder systems with the loading surface (11) makes necessary to use more complex forms of the loading surface.

Figure 7 demonstrates the monotonic loading curves of systems I and II, corresponding to the modeled processes A–D, in the space of the stress tensor invariants and the dependences $\tau_c(p_c)$ characterizing the shear deformation process (E). The states corresponding to the constant values of the unloading density ρ_u are marked by the points on the curves. We can see that position of these points requires at least displacement of the loading ellipse towards positive values of p . Therefore, we can represent the loading surface equation in the form of

$$(p - p_0)^2 + \tau^2 q_1(\theta) = q_2(\theta, \Gamma_0) . \quad (18)$$

As a first approximation, we can assume that all three unknown parameters (p_0 , q_1 and q_2) depend only on the porosity. Then it is not a problem to determine them from any three points corresponding to the constant porosity values. Loading surfaces constructed in this way for system II at density values $\rho_u = 0.60$ and 0.62 are shown in Fig. 7 to the right (dashed lines). The points of the processes A, B, and C are used for their construction. We can see that continuations of the constructed ellipses do not reach the corresponding points on the lines of D and E processes. This can be connected with the neglect of the dependence of the parameter q_2 on the accumulated effective strain Γ_0 . The transition from the process A (uniform compression) to the curves $\tau(p)$ of the processes B–E along the constant density lines corresponds to the increase of the shear deformation contribution. This should lead to growth of the values Γ_0 and, therefore, increase the ellipse "dimension". Thus, taking into account the influence of the accumulated strain (Γ_0), we can describe all represented processes by the "shifted ellipse" surface (18).

With the aim of indirect taking into account the dependence of the parameter q_2 on the compaction condi-

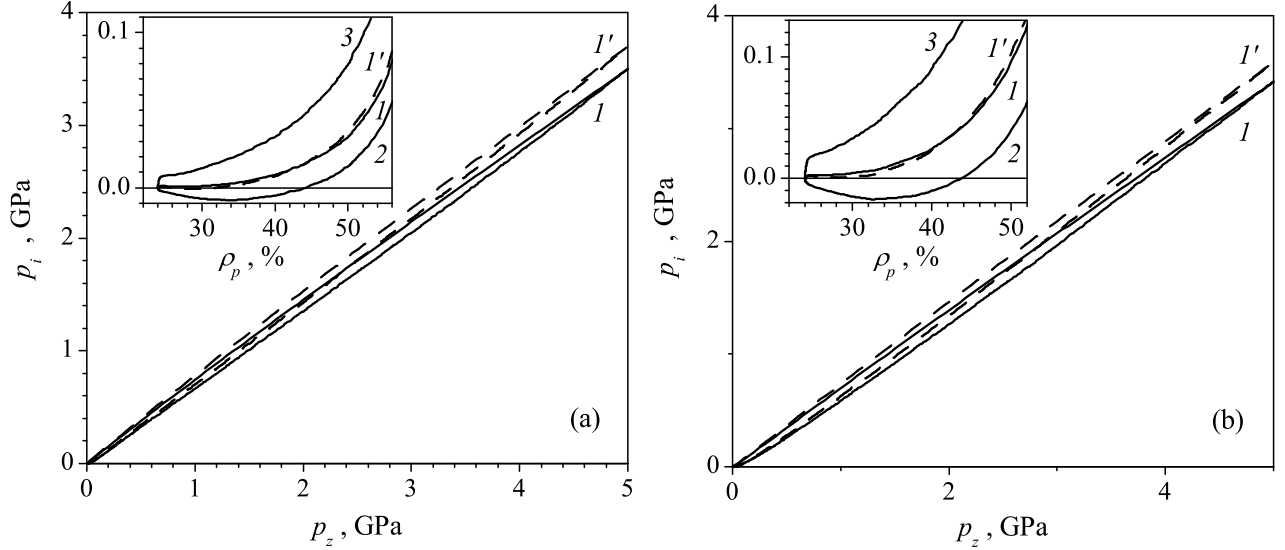


Figure 8: Calculated values of the stresses along Ox axis ($p_x = -\sigma_{xx}$, solid lines 1) and values of $p_x^{(as)}$ corresponding to the associated flow rule (Eq. (20), dashed lines 1') for the process D in the systems I (a) and II (b). The lines of monotonic loading up to $p_z = 5$ GPa and elastic unloading are shown. The insets show the values $p_x / 1$, $p_x^{(as)} / 1'$, $p_y / 2$, and $p_z / 3$ versus density ρ_p in the low pressure zone.

tions, the following approximation of loading surface was applied

$$(p - p_0)^2 + \tau^2 q_1(\theta) = (p_A - p_0)^2 [1 + \alpha (p_A - p)^m] . \quad (19)$$

Here p_A is the value of p on the A-line, that is the maximum value p for a given density; p_0 , q_1 , α , and m are the parameters depending on the density (porosity). This approximation due to the second term in the square brackets takes into account increasing of the ellipse "dimensions" during transition from the A-process to B, C and so on. The results of applying the formula (19) are represented in Fig. 7 by dotted lines. It was accepted in this case for all density values that $p_0 = 0.7p_A$ and remaining parameters were determined from the condition of the best describing the points B, C, D and E. Figure 7 shows that the approximation (19) allows us to reproduce accurately enough all calculation points besides the line E (simple shear). Before passing through the corresponding point on the E-process curve, the constant density line crosses the curve E in the region of larger density values. The latter, in our view, indicates the end of the loading surface in the E-line neighborhood. If we neglect the strain hardening contribution to the strain resistance of the examined powder systems, the E-line can be associated with the fracture surface of the model systems. This qualitatively corresponds with the data [29] on this boundary location. It should be noted that the E-line in the system I closely coincides with the D-process curve. Therefore constructed loading surfaces end at the D-line.

VI. Associated flow rule

The loading surface, constructed in the previous section, allows us to test the applicability of the associated flow rule to description of the nanopowder behavior. One implication of the associated flow rule is the deviator coaxiality for the stress and strain rate tensors, that is $\tau_{ij} \propto \gamma_{ij}$. It is not difficult to determine that in the cases of A, B, and C processes the feasibility of the coaxiality is ensured by the symmetry condition, i.e., the equality of stresses along the directions with equal strain rates. This fact is not difficult to prove in common case. Let principal axes of the both tensors coincide (that is, in our case, the material is isotropic) and two diagonal elements are equal. Lets take for definiteness that $\sigma_1 = \sigma_2 \neq \sigma_3$ and $e_1 = e_2 \neq e_3$. Then the deviator components of these tensors can be found as $\tau_1 = \tau_2 = -\tau_3/2$ and $\gamma_1 = \gamma_2 = -\gamma_3/2$. That means that the deviators are coaxial.

In the cases of D (compression with shear deformation) and E (simple shear) processes the coaxiality of the stress deviator to the strain rate deviator leads to the need of following relations between stress tensor components:

$$\mathbf{D} : p_x^{(as)} = (2p_y + p_z)/3 ; \quad \mathbf{E} : p_x^{(as)} = (p_y + p_z)/2 . \quad (20)$$

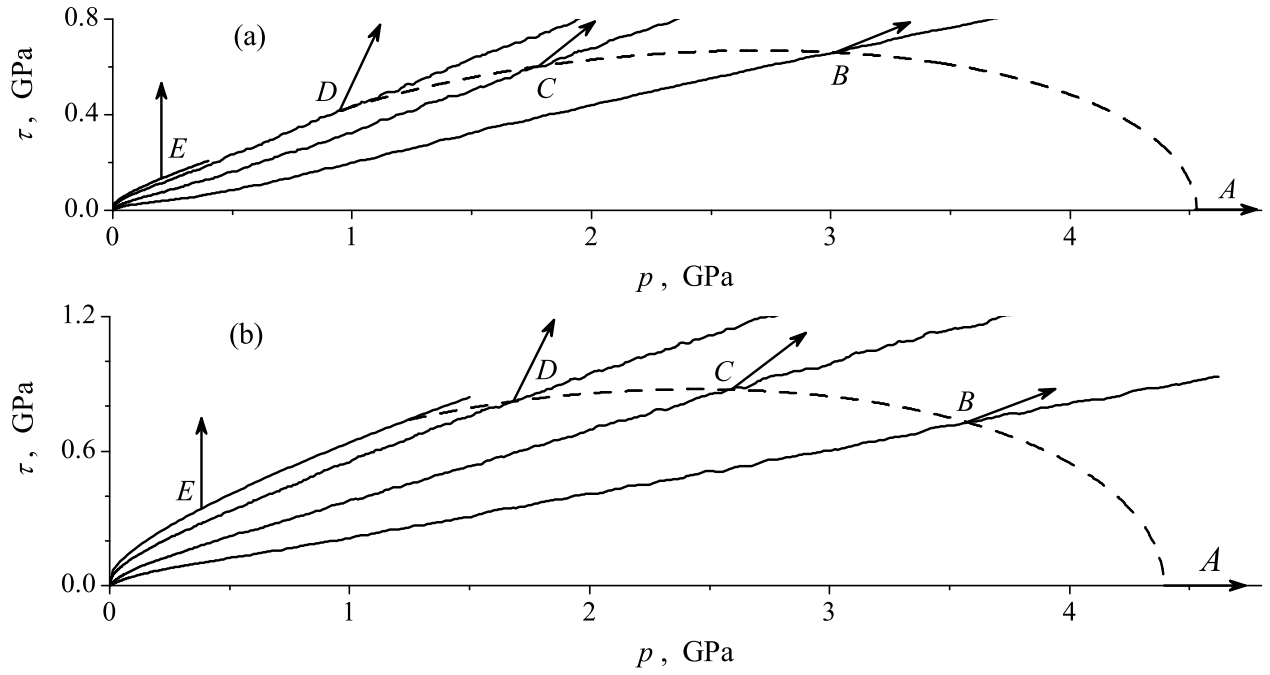


Figure 9: Stress deviator intensity versus hydrostatic pressure for systems I (above) and II (below). Solid lines correspond to the processes A–E (line A coincides with the abscissa axis), dashed line is the loading surface (19) at value $\rho_u = 61.6\%$ in the system I and 62.0% in the system II. Arrows represent the vectors (e, γ) defining strain "direction" in the processes A–E (here the positive value e corresponds to the compression).

Figure 8 demonstrates rather good coincidence of the calculated values p_x with the value $p_x^{(as)}$ in the D-process case. This can be considered as the confirmation of the associated flow rule. For instance, at $p_z = 5$ GPa the difference between p_x and $p_x^{(as)}$ is about 6% in both systems. This difference in the whole pressure range is significantly smaller than differences between separate components of the stress tensor (see insets in Fig. 8). In the case of E-process the difference between p_x and $p_x^{(as)}$ is rather larger: it reaches 14% from the difference $p_z - p_y$. This fact can be related to the particular status of the E-process that was discussed in the previous section, namely, closeness or even identity of the E-process with the fracture surface of powder body.

Another implication of the associated flow rule, in addition to the coaxiality of the tensors τ_{ij} and γ_{ij} , is the orthogonality of the vector (e, γ) , which specifies the "direction" of the deformation process, to the loading surface in the $p - \tau$ plane. In particular, it leads to the scalar relation (13) for the elliptic-type surface (11). Figure 9 presents the loading surfaces corresponding to the densities $\rho = 61.6\%$ and 62.0% for the systems I and II, respectively, and also the vectors (e, γ) characterizing the A–E processes. We can see that the orthogonality to the loading surface is observed only in the trivial case of the uniform compression (the line of A-process, which coincides with the abscissa axis). All other vectors noticeably deviate from the normal to larger values e , that is, the material demonstrates too high densification rate in comparison with the associated flow rule for given stresses. For example, the positions of the points C and D on the loading surface of I system and the points D on the loading surface of II system indicate a need for density decrease in this processes. This fundamentally contradicts to the conducted numerical experiments where the processes C and D have corresponded to the density increase.

Thus, we can establish the nonapplicability of the associated flow rule to the mechanical properties description of the oxide nanopowders due to the failure of one of its implications (the orthogonality of the vector (e, γ) to the loading surface). The non-orthogonality of the vectors (e, γ) to the loading surface is observed more appreciable for the system I which has no hard interparticle bonds. Appearance of such bonds in the system II makes it more similar to the behavior of a plastic porous body. This deviation from the orthogonality principle occurs rather often in the mechanics of granulated solids and soils. Therefore, a number of authors prefer to introduce the loading surface and the plastic potential independently of each other [38, 39, 40]. The need for the plastic potential introduction is explained by the fact that it determines the relations between stresses and strain rates in the plastic material. This provides the possibility to formulate and solve initial boundary value problems. Furthermore, the presence of potential ensures the variational principle implementation that

simplifies significantly numerical solution procedures.

Factors contributing to the non-orthogonality of the vectors (e, γ) to the loading surface include, first of all, lack of comprehensive information on tolerance for the plastic strain. Here it should be taking into account that the energy dissipation in the examined systems has a very low threshold. Therefore, the insignificant residual strains in powder systems as well as in granulated solids and soils are already observed on the prime deformation stage. Moreover, the relative irreversibility threshold can be sensitive to the loading path, as experimental data show.

VII. Conclusion

The main results of the study are as follows.

1. The two granular systems corresponding oxide nanopowders have been examined by the granular dynamics method. The I system, which has no hard interparticle bonds of chemical nature, corresponds to the non-agglomerating nanopowders because of layers of adsorbed gases on the particles. The II system, which includes creation and destruction of hard bonds, corresponds to the purified nanopowders strongly inclined to agglomeration. For these systems the quasistatic processes of the uniaxial, biaxial, uniform compression and the compression with shear deformation of the model cell have been simulated. The elasto-reversible contribution mainly connecting with the elastic strain of individual particles and the plastic irreversible contribution connecting with mutual displacements of particles have been extracted from the total deformation. The plastic part of the deformation is characterized by the unloading density ρ_u . It has been determined that in the coordinates $\ln(p_{out}) - \rho_u$, where p_{out} is the maximal external pressure, the curves of all examined processes are close to each other for densification from the equal initial density ($\rho_0 = 24\%$). The density differences are less than 2%. The final powder state in the high pressure range is close to the parameters of random close packing, i.e., the density $\rho \simeq 64\%$, the coordination number $k \simeq 6$. On the compaction curves $p_{out}(\rho_u)$ we can identify three stages: 1) the stage of insignificant density change with pressure increasing, when the external loading is insufficient to overcome the initial particle bonds; 2) the stage of "logarithmic" densification ($\Delta\rho \propto \ln(p_{out})$), when the intensive particle rearrangement occurs; 3) the stage when the density tends to some maximum value ρ_{max} . For third stage the dependence $p_{out} \propto 1/(\rho_{max} - \rho)^{D-1}$ has been established, where D is the space dimension.

2. The oxide nanopowder behavior under shear deformation has been simulated. Here the effect of the positive dilatancy has been found out: the examined systems tend to increase their volume under the simple shear stress. In simulation results (at constant volume) this fact appears as positive values of the hydrostatic pressure p_c . As the density grows the dilatancy increases too. Whereas the pressure p_c is significantly lower than the tangential stress level τ_c at densities $\rho < 50\%$, we have already $p_c > \tau_c$ at high densities ($\rho > 60\%$). Comparison of examined systems I and II shows that the appearance of hard bonds significantly increases the dilatancy in the low density range ($\rho < 50\%$). But qualitatively the properties of both systems are similar. This fact allows us to conclude that the main reason of the positive dilatancy in whole investigated density range is the high dispersive attraction forces inherent to nanopowders.

3. The approximating formula for the loading surfaces of the examined systems has been offered. It has been established that these surfaces are close to the elliptic-type surface. However, the loading ellipse in the $p - \tau$ plane is strongly shifted towards positive values of p and its shape is determined by not only the powder porosity but also the specific features of loading. The suggested approximation of the loading surface allows us to reproduce satisfactorily all examined processes except for the shear deformation of the model cell (E-process). It has been identified that before passing through the corresponding point on the E-process curve (in the $p - \tau$ plane) the constant density line crosses the curve E in the region of larger density values. The latter can indicate the end of the loading surface in the E-line neighborhood. Based on this fact we can conclude that the E-process curve can be associated with the fracture surface of the systems examined.

4. The nonapplicability of the associated flow rule to the mechanical properties description of the oxide nanopowders has been found out. At the same time, one implication of the associated flow rule, that is the deviator coaxiality of the stress and strain rate tensors, remains valid. But another implication, that is the orthogonality of the vectors (e, γ) to the loading surface in the $p - \tau$ plane, is broken. This fact indicates that the loading surface for the oxide nanopowders does not coincide with the plastic potential isolevels and, therefore, cannot be used for the estimation of the system dissipative behavior.

The work is supported by the RFBR, projects 12-08-00298 and 14-08-90404.

References

- [1] R.W. Siegel, *Nanostructured Materials* **4**, 121 (1994).
- [2] V.V. Ivanov, V.R. Khrustov, S.N. Pararin, A.I. Medvedev, A.K. Shtol'ts, O.F. Ivanova, and A.A. Nozdrin, *Glass Physics and Chemistry* **31**, No. 4, 465 (2005).
- [3] Ivanov V.V., Kaygorodov A.S., Khrustov V.R., Pararin S.N., Spirin A.V. Hard alumina-based ceramics fabricated by the use of magnetic pulsed compaction of composite nanopowders // *Russian Nanotechnologies*. 2006. V. 1. No 1-2. P. 201-207.
- [4] V.R. Khrustov, V.V. Ivanov, Yu.A. Kotov, A.S. Kaigorodov, and O.F. Ivanova, *Glass Physics and Chemistry* **33**, 379 (2007).
- [5] Kaygorodov A.S., Ivanov V.V., Khrustov V.R., Kotov Yu.A., Medvedev A.I., Osipov V.V., Ivanov M.G., Orlov A.N., Murzakaev A.M. Fabrication of Nd:Y₂O₃ transparent ceramics by pulsed compaction and sintering of weakly agglomerated nanopowders // *Journal of the European Ceramic Society*. 2007. V. 27, Iss. 2-3. P. 1165-1169.
- [6] M.B. Shtern, G.G. Serdyuk, L.A. Maksimenko, Yu.V. Truhan, and Yu.M. Shulyakov, *Phenomenological Theories of Powder Pressing* [in Russian], Naukova Dumka, Kiev (1982).
- [7] G.Sh. Boltachev, K.A. Nagayev, S.N. Pararin, A.V. Spirin, and N.B. Volkov, *Magnetic Pulsed Compaction of Nanosized Powders*. NY, Nova Science Publishers, Inc., 2010.
- [8] V.P. Filonenko, L.G. Khvostantsev, R.Kh. Bagramov, L.I. Trusov, and V.I. Novikov, *Powder Metallurgy and Metal Ceramics*. 1992. V. 31, No. 4. P. 296-299.
- [9] R. Vassen and D. Stöver, *Powder Technology*. 1992. V. 72. P. 223-226.
- [10] M. Zhao, X. Li, Z. Wang, L. Song, L. Xiao, and B. Xu, *NanoStructured Materials*. 1992. V. 1, No. 5. P. 379-386.
- [11] B.P. Saha, V. Kumar, S.V. Joshi, A. Balakrishnan, and C.L. Martin, *Powder Technology*. 2012. V. 224. P. 90-95.
- [12] A. Balakrishnan, P. Pizette, C.L. Martin, S.V. Joshi, and B.P. Saha, *Acta Materialia*. 2010. V. 58. P. 802-812.
- [13] G.Sh. Boltachev and N.B. Volkov, *Technical Physics*. 2011. V. 56, No. 7. P. 919-930.
- [14] G.Sh. Boltachev, N.B. Volkov, A.S. Kaygorodov, and V.P. Loznukho, *Nanotechnologies in Russia*. 2011. V. 6, No. 9-10. P. 639-646.
- [15] G.Sh. Boltachev, K.E. Lukyashin, V.A. Shitov, and N.B. Volkov, *Phys. Rev. E*. 2013. V. 88, No. 1. 012209.
- [16] Olevsky E.A., Bokov A.A., Boltachev G.Sh., Volkov N.B., Zayats S.V., Ilyina A.M., Nozdrin A.A., Pararin S.N. Modeling and optimization of uniaxial magnetic pulse compaction of nanopowders // *Acta Mechanica* 2013. V. 224, Iss. 12. P. 3177-3195.
- [17] A.L. Maximenko, E.A. Olevsky, and M.B. Shtern, *Computational Materials Science*. 2008. V. 43. P. 704-709.
- [18] V.V. Skorokhod, *Rheological Principles of Sintering Theory* [in Russian], Naukova Dumka, Kiev (1972).
- [19] E.A. Olevskii and M.B. Shtern, *Powder Metallurgy and Metal Ceramics*. 2004. V. 43, No. 7-8. P. 355-363.
- [20] V.G. Gryaznov, A.M. Kaprelov, and A.E. Romanov, *Pisma v Zhurnal Tekhnicheskoi Fiziki (Technical Physics Letters)*. 1989. V. 15, Iss. 2. P. 39-44.
- [21] P.A. Cundall and O.D.L. Strack, *Geotechnique*. 1979. V. 29, No 1. P. 47-65.
- [22] I. Agnolin and J.-N. Roux, *Phys. Rev. E* 76. 2007. 061302.
- [23] F.A. Gilabert, J.-N. Roux, and A. Castellanos, *Phys. Rev. E*. 2007. V. 75. 011303 (26 pages).

- [24] F.A. Gilabert, J.-N. Roux, and A. Castellanos, *Phys. Rev. E*. 2008. V. 78. 031305 (21 pages).
- [25] H.P. Zhu, Z.Y. Zhou, R.Y. Yang, and A.B. Yu, *Chem. Eng. Sci.* 2008. V. 63, Iss. 23. P. 5728-5770.
- [26] Luding S. Cohesive, frictional powders: contact models for tension // *Granular Matter*. 2008. V. 10. P. 235-246.
- [27] Salot C., Gotteland P., Villard P. Influence of relative density on granular materials behavior: DEM simulations of triaxial tests // *Granular Matter*. 2009. V. 11. P. 221-236.
- [28] Teufelsbauer H., Wang Y., Chiou M. -C., Wu W. Flow-obstacle interaction in rapid granular avalanches: DEM simulation and comparison with experiment // *Granular Matter*. 2009. V. 11. P. 209-220.
- [29] P. Pizette, C.L. Martin, G. Delette, P. Sornay, and F. Sans, *Powder Technology*. 2010. V. 198. P. 240-250.
- [30] Yang J., Wu C.-Y., Adams M. DEM analysis of particle adhesion during powder mixing for dry powder inhaler formulation development // *Granular Matter*. 2013. V. 15. P. 417-426.
- [31] E. Reissner and H.F. Sagoci, *J. Appl. Phys.* 1944. V. 15, No. 9. P. 652-654.
- [32] A.I. Lur'e, *Three-Dimensional Problems of the Theory of Elasticity* (NY, Interscience Publishers, 1964).
- [33] A. Castellanos, *Advances in Physics*. 2005. V. 54, No. 4. P. 263-376.
- [34] Valverde J.M., Castellanos A. Compaction of fine powders: from fluidized agglomerates to primary particles // *Granular Matter*. 2007. V. 9. P. 19-24.
- [35] G.Sh. Boltachev and N.B. Volkov, *Powder Metallurgy and Metal Ceramics*. 2012. V. 51, No. 5-6. P. 260-266.
- [36] A.S. Povarennykh, *Mineral hardness* [in Russian]. Kiev: Izdat. AN Ukrainian SSR, 1963.
- [37] G.Sh. Boltachev, N.B. Volkov, S.V. Dobrov, V.V. Ivanov, A.A. Nozdrin, and S.N. Paranin, *Technical Physics*, 2007, Vol. 52, No. 10, pp. 1306-1315.
- [38] J.W. Rudnicki and J.R. Rice, *Journal of the Mechanics and Physics of Solids*. 1975. V. 23. P. 371-394.
- [39] I.A. Garagash and V.N. Nikolayevskii, *Usp. Mekh.* 1989. V. 12, Iss. 1. P. 131-183.
- [40] D.J. Holcomb and J.W. Rudnicki, *Int. J. Numer. Anal. Meth. Geomech.* 2001. V. 25. P. 109-129.